C. R. Mecanique 346 (2018) 844–854

Contents lists available at ScienceDirect

Comptes Rendus Mecanique

www.sciencedirect.com

Separated nozzle flow

Abderrahmane Nebbache

INSA de Rouen, LMFN–CORIA, UMR CNRS 6614, 76801 Saint-Étienne-du-Rouvray, France

ARTICLE INFO

Article history:
Received 19 March 2018
Accepted 9 June 2018
Available online 29 June 2018

Keywords:
Supersonic
Compressible
Nozzle flow
Axisymmetrical shock separation
Turbulence
URANS approach

ABSTRACT

A separated turbulent flow in an axisymmetrical nozzle is studied numerically. Two configurations nozzle are investigated. The first one is the truncated ideal contour nozzle, DLR-TIC, is fed with nitrogen. The second configuration is called the thrust optimized contour nozzle or TOC type, ONERA-TOC, where the operating gas is a hot air. The classical pattern of a free shock separation is obtained for different values of the nozzle pressure ratio. The results are compared and validated using experimental data.

1. Introduction

The objective of this work is to simulate the turbulent nozzle flow. The ONERA-TOC nozzle without wall film cooling and the DLR-TIC nozzle are the configuration of the nozzle that are studied. The ONERA-TOC nozzle is like a nozzle of the Vulcain-2 rocket engine, which has downstream of its throat section a system to inject wall film cooling.

The ONERA-TOC nozzle is subject to flow separation in transient phase at start-up or shut-down. This separation phenomenon can also appear in overexpanded nozzle flow at a fixed nozzle pressure ratio (NPR), where $NPR = p_c/p_a$ (p_c and p_a are respectively the chamber and the ambient pressure). The flow issued from the TOC nozzle exhibits two different kinds of separation patterns for a certain range of pressure ratio. The first separation pattern is obtained when the separated flow continues as a free jet. In this case, the separation region extends from the separation point downwards the nozzle's exit. This separation pattern is called free shock separation (FSS). This FSS pattern can be obtained in many different geometries of nozzles, and was reported in many publications dating from the 1950s and 1960s. The FSS pattern appears in thrust optimized contour nozzles for low pressure ratios p_c/p_a. The second separation pattern type, which is called the restricted shock separation (RSS), appears in the TOC nozzle for a high pressure ratio. In this separation pattern, the flow is reattached to the wall downstream of the separation point, forming a closed recirculation bubble. Moreover, the separation pattern evolves from a free shock separation to a restricted shock separation when the pressure ratio increases. Transitions between these two kinds of separation pattern present an hysteresis phenomenon. High peaks of side load are observed during transitions from FSS to RSS and back. This hysteresis phenomenon appears typically during the start-up and the shut-down process. The transition FSS $\Rightarrow$ RSS occurs for a pressure ratio value that is higher than the one observed for the RSS/FSS transition.

This phenomenon, still imperfectly understood, was observed in many TOC nozzles. Experimental or numerical tests highlighted it, not only in subscale models supplied with cold air [10], [8], [3] and [11], but also, more recently, in rocket nozzles on real scale with hot gases. Onofri and Nasuti [12], like Frey and Hagemann [9], have observed it numerically in

E-mail address: abderrahmane.nebbache@insa-rouen.fr.

https://doi.org/10.1016/j.crme.2018.06.009

the nozzle of Vulcain engine. In thrust-optimized contour nozzles, a weak internal shock is induced in the throat region, where the circular arc forming the nozzle throat turns into the further expansion contour. The role of this internal shock seems essential in the set up of a particular shock structure that is called by European engineers *cap shock*. This pattern is observed in the plume of the axisymmetric nozzle of Vulcain engine. This shock structure deflects the flow and the slip line away from the nozzle's axis, whereas the free shock separation pattern leads to the classical Mach reflection, where the slip line and the flow were deflecting towards the nozzle's axis. The restricted shock separation with the cap shock pattern was confirmed by the Navier–Stokes computations [8], [9], [12] and [3], which show, at the steady state, the presence of a recirculating core behind the Mach disk. The existence of the vortex behind the Mach disk has been confirmed experimentally by a laser velocimetry campaign on the plume of an axisymmetrical onera-toc nozzle tested in the ONERA-R2Ch wind tunnel [13]. This presence of the recirculation bubble behind the Mach disk can be conveniently interpreted as a reaction of the flow to insure that the static pressure is always lower than the stagnation pressure [13]. This flow structure is associated with an inverse Mach reflection process of internal shock [13].

The experimental or numerical overexpanded LEA-TIC nozzle flow studies [1] and [2] use cold dry air as operating gas at a stagnation temperature close to 270 K. For high nozzle pressure ratios ($NPR > 30$), the condensation phenomenon of oxygen appears in a region located behind the separation shock structure. Therefore, the flow becomes a two-phase one. In this condition, the perfect gas hypothesis is not fully valid. The two-dimensional axisymmetric numerical code used in that study does not take the effect of condensation into account. Nevertheless, the numerical results show wall pressure and separation point location distributions in reasonable agreement with measurements until the condensation of oxygen of air begins.

This calculation code does not deal with two-phase flows. At ONERA ("Office national d'études et de recherches aérospatiales") and DLR ("Deutsches Zentrum für Luft- und Raumfahrt"), experiments or numerical simulations on nozzle flows use hot air to avoid the condensation of oxygen occurring in the divergent nozzle.

Nevertheless, let us note that among the works relating to the two-phase flow, there is the study of I. Shih Chang [16] concerning the numerical simulation of a two-phase flow, gas-particle, in a nozzle. This work follows the need for a better understanding of the flow in rocket engine nozzle that uses a solid propellant. The combustion products are then burned gases and solid particles. The gas burned is supposed to be inviscid. The volume occupied by solid particles is assumed to be very low. The numerical scheme used is that of MacCormack [17].

The present paper concerns a separated turbulent flow in an axisymmetrical nozzle both DLR-TIC and ONERA-TOC without film injection. The gas operating used in the DLR-TIC nozzle is nitrogen. The ONERA-TOC nozzle flow is fed with hot air. The study of this turbulent nozzle flow has been carried out by solving the Reynolds averaged Navier–Stokes equations. The numerical method that is used is the two-stage explicit–implicit finite volume method developed by MacCormack [4]. The accuracy of this predictor–corrector method is second order in time and space. Turbulence is modeled by the two-equation $k-\omega$ Shear–Stress–Transport (SST) approach of Menter [5].

2. Viscosity and the fluid operating

The fluid operating is assumed to obey the perfect gas law ($p=\rho r T$). The isentropic exponent of nitrogen or air is $\gamma=1.4$. The gas constants are set to $r=\frac{\mathbf{R}}{\mathbf{M}}=297.0\ \mathrm{J{\cdot}kg^{-1}{\cdot}K^{-1}}$ for nitrogen and $r=287\ \mathrm{J{\cdot}kg^{-1}{\cdot}K^{-1}}$ for air.

The molecular viscosity μ of air varies with temperature T. It is given by the Sutherland law as:

$$\mu=\mu_0\sqrt{\frac{T}{T_0}}\frac{(1+S/T_0)}{(1+S/T)}$$

with $\mu_0=1.716\times10^{-5}\ \mathrm{kg{\cdot}m^{-1}{\cdot}s^{-1}}$, the molecular viscosity at reference temperature $T_0=273$ K, and $S=111$ K.

The molecular viscosity of nitrogen varies also with temperature T, and it is computed as:

$$\mu=0.694909\ 10^{-4}\left(1+0.323\log\left(\frac{T}{91.46}\right)\right)\sqrt{\frac{T}{91.46}}$$

3. Computational domain and boundary conditions

For the two nozzle configurations, DLR-TIC and ONERA-TOC, the axisymmetrical domain (Figs. 4 and 5) is splitted into three parts: nozzle, jet, and bottom domain.

The sketch of the computational domain (see Fig. 5) shows the profile of the ONERA-TOC nozzle, which represents a kind of backward-facing step in its divergent. R_{exit} is the radius of the nozzle's exit. Along the nozzle wall or walls Σ_1, Σ_2, and Σ_3, the no-slip condition is assumed. These walls are considered to be adiabatic. The normal pressure gradient at these walls is close to zero. At the wall, the turbulent quantities are:

$$k=0\quad;\quad\omega=\frac{60\nu_w}{\beta_1 y_{\mathrm{n}_1}^2}\quad;\quad\beta_1=0.075$$

where ν_w is the kinematic viscosity at the wall, y_{n_1} is the distance from the wall to the first point of the mesh and β_1 is one of constants SST–Menter's model.

The boundary Σ_4 is treated as a far field inflow, with small velocities. Temperature and pressure evolutions from the ambient state are then assumed to be isentropic. Velocities are extrapolated and the normal derivative for all other dependent variables are required to vanish. The symmetry axis is considered as a slip line. The subsonic inflow boundary condition Σ_0 is assumed to be nearly fully laminar, so that $\sqrt{k_\infty}/U_\infty = 3 \times 10^{-4}$ and the turbulent Reynolds number is $Re_\mathrm{t} = 10^{-7}$. The values of k_∞ and ω_∞, which are chosen and imposed at the inlet of the nozzle (Σ_0), do not influence the core flow solution. These selected turbulent quantities contribute to stabilize the computation, especially in the convergent part of the nozzle, where the flow is subsonic. Along the subsonic boundary Σ_0, the value of the other dependent variables were found by extrapolation based on the method of characteristics. This method of characteristics is also used to obtain the subsonic or supersonic outflow boundary Σ_5 values.

3.1. The subsonic or supersonic outflow boundary Σ_5

The characteristic form of the system of one-dimensional Euler equations (I) can be written as [15]:

$$
(I)\ \begin{cases}
\frac{\partial \rho}{\partial t} - \frac{1}{c^2}\frac{\partial p}{\partial t} = -u\left(\frac{\partial \rho}{\partial x} - \frac{1}{c^2}\frac{\partial p}{\partial x}\right) \\
\frac{\partial p}{\partial t} + \rho c\frac{\partial u}{\partial t} = -(u+c)\left(\frac{\partial p}{\partial x} + \rho c\frac{\partial u}{\partial x}\right) \\
\frac{\partial v}{\partial t} = -u\frac{\partial v}{\partial x} \\
\frac{\partial p}{\partial t} - \rho c\frac{\partial u}{\partial t} = -(u-c)\left(\frac{\partial p}{\partial x} - \rho c\frac{\partial u}{\partial x}\right) \\
\frac{\partial k}{\partial t} = -u\frac{\partial k}{\partial x} \\
\frac{\partial \epsilon}{\partial t} = -u\frac{\partial \epsilon}{\partial x}
\end{cases}
$$

c is the speed of sound, p is pressure, ρ is density, u and v are the x and velocity components, k is the kinetic energy of turbulence, and ϵ is the dissipation rate of the kinetic energy of turbulence.

Note that only the time t and the x spatial derivatives are retained. It is also assumed that the exit boundary (Σ_5) is located in a region where the y spatial derivatives are negligible.

This system (I) can be decoupled into characteristic variables w and written as:

$$
\frac{\partial w}{\partial t} + \Lambda\frac{\partial w}{\partial x} = 0\,;\ \Lambda = \begin{pmatrix} u & 0 & 0 & 0 & 0 & 0 \\ 0 & u+c & 0 & 0 & 0 & 0 \\ 0 & 0 & u & 0 & 0 & 0 \\ 0 & 0 & 0 & u-c & 0 & 0 \\ 0 & 0 & 0 & 0 & u & 0 \\ 0 & 0 & 0 & 0 & 0 & u \end{pmatrix} \tag{1}
$$

The characteristic variables are written as:

$$
\delta w = \begin{cases} \delta\rho - \frac{1}{c^2}\delta p \\ \delta p + \rho c\delta u \\ \delta v \\ \delta p - \rho c\delta u \\ \delta k \\ \delta\epsilon \end{cases}
$$

Fig. 1 shows the characteristic lines for a one-dimensional flow. On a characteristic line, the flow quantities $(p, \rho, u, c, \ldots)$ are constant, this characteristic can be assimilated to a Mach line. The tangents to the characteristic line c_0, c_+ and c_- have, respectively, slopes $(\mathrm{d}x/\mathrm{d}t)$ equal to u, $u+c$, and $u-c$, respectively. The characteristic variables $\delta\rho - \frac{1}{c^2}\delta p$, $\delta p + \rho c\delta u$ and $\delta p - \rho c\delta u$, respectively, propagate with velocity u, $u+c$ and $u-c$ along the characteristics C_0, C_+, and C_-, respectively. When the flow is supersonic, the characteristics C_0, C_+ and C_- are oriented in the direction of the flow because their slopes are positive (see Fig. 3). The slope of C_- is negative when the flow is subsonic. In this way, the characteristic C_- is oriented from downstream to upstream of the flow (see Fig. 2). Taking into account the characteristic relations leads to the calculation of the flow quantities at the downstream boundary, which can be supersonic or subsonic.

It should be noted that the system (1) consists of 6 one-dimensional wave propagation equations:

$$
\frac{\partial wk}{\partial t} + \lambda_k\frac{\partial wk}{\partial x} = 0 \tag{2}
$$

Implicit finite difference approximations for (2) lead to:

$$
wk_i^{n+1} = wk_i^n - \lambda_h(wk_i^{n+1} - wk_{i-1}^{n+1})\,;\ \lambda_h = \lambda_k\frac{\Delta t}{\Delta x}
$$

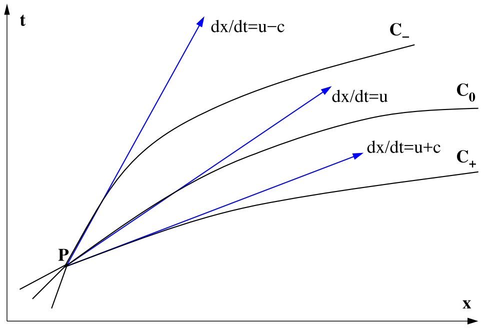

Fig. 1. Characteristic lines.

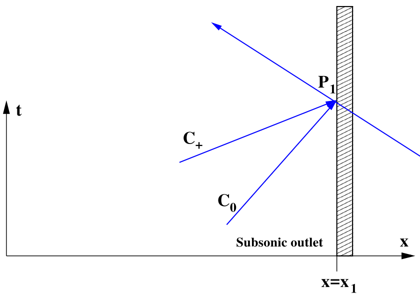

Fig. 2. Subsonic exit boundary.

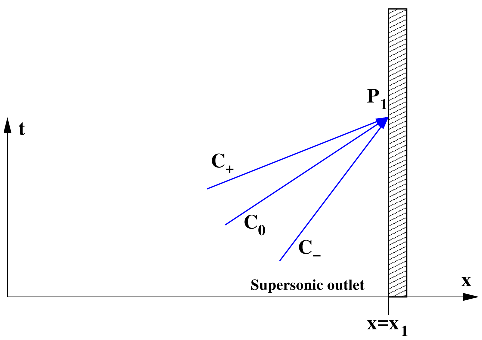

Fig. 3. Supersonic exit boundary.

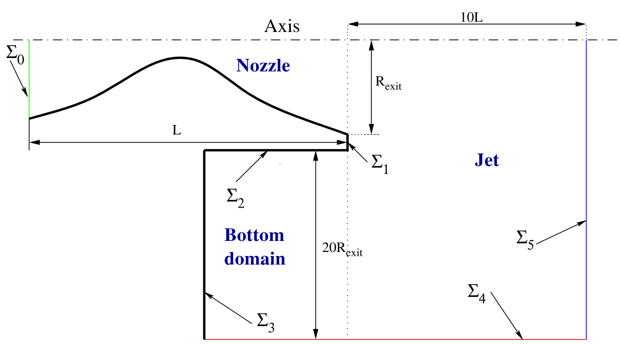

Fig. 4. Axisymmetrical computed domain for DLR-TIC.

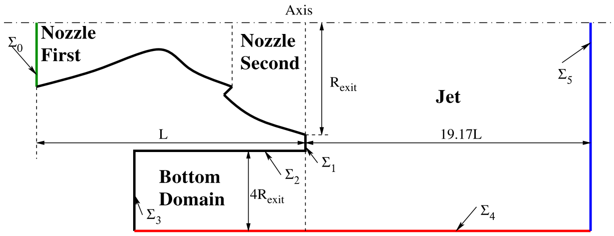

Fig. 5. Axisymmetrical computed domain for ONERA-TOC.

$$wk_i^{n+1} = \frac{1}{1+\lambda_h} wk_i^n + \frac{\lambda_h}{1+\lambda_h} wk_{i-1}^{n+1}$$

and

$$\begin{aligned} \delta wk_i &= wk_i^{n+1} - wk_i^n \\ &= \frac{1}{1+\lambda_h} wk_i^n + \frac{\lambda_h}{1+\lambda_h} wk_{i-1}^{n+1} - wk_i^n \\ &= -\frac{\lambda_h}{1+\lambda_h}(wk_i^n - wk_{i-1}^{n+1}) \end{aligned}$$

Assume that p_∞ is specified if the flow at the exit (Σ_5 corresponding at increment IL) is subsonic. The six characteristic equations connecting points (IL, j) and $(IL-1, j)$ at the exit are:

$$\begin{cases} \delta\rho - \frac{1}{c^2}\delta p = -\frac{\lambda_1}{1+\lambda_1}\left(\rho_{IL} - \rho_{IL-1} - \frac{1}{c^2}\big(p_{IL} - p_{IL-1}\big)\right) = R_1 \\ \delta p + \rho c \delta u = -\frac{\lambda_2}{1+\lambda_2}\left(p_{IL} - p_{IL-1} + \rho c\big(u_{IL} - u_{IL-1}\big)\right) = R_2 \\ \delta v = -\frac{\lambda_1}{1+\lambda_1}\big(v_{IL} - v_{IL-1}\big) = R_3 \\ \delta p - \rho c \delta u = -\frac{\lambda_4}{1+\lambda_4}\left(p_{IL} - p_{IL-1} - \rho c\big(u_{IL} - u_{IL-1}\big)\right) = R_4 \\ \delta k = -\frac{\lambda_1}{1+\lambda_1}\big(k_{IL} - k_{IL-1}\big) = R_5 \\ \delta\epsilon = -\frac{\lambda_1}{1+\lambda_1}\big(\epsilon_{IL} - \epsilon_{IL-1}\big) = R_6 \end{cases}$$

λ_1, λ_2 and λ_4 are:

$$\lambda_1 = u\frac{\Delta t}{\Delta x}\ ;\ \lambda_2 = (u+c)\frac{\Delta t}{\Delta x}\ ;\ \lambda_4 = (u-c)\frac{\Delta t}{\Delta x}$$

δp is obtained as:

$$\delta p = \begin{cases} \frac{R_2+R_4}{2} \quad \text{if} \quad M = \frac{u_{IL-1}}{c_{IL-1}} > 1 \\ 0 \quad \text{if} \quad M = \frac{u_{IL-1}}{c_{IL-1}} < 1 \quad \left(\text{assuming } \frac{\partial p_\infty}{\partial t} = 0\right) \end{cases}$$

and:

$$\begin{cases} \delta\rho = R_1 + \frac{\delta p}{c^2} \\ \delta u = \frac{R_2 - \delta p}{\rho c} \\ \delta v = R_3 \\ \delta k = R_5 \\ \delta\epsilon = R_6 \end{cases}$$

and, finally, the flow field variables at (Σ_5) are:

$$\begin{cases} p_{IL}^{n+1} = p_{IL}^n + \delta p \\ \rho_{IL}^{n+1} = \rho_{IL}^n + \delta\rho \\ u_{IL}^{n+1} = u_{IL}^n + \delta u \\ v_{IL}^{n+1} = v_{IL}^n + \delta v \\ k_{IL}^{n+1} = k_{IL}^n + \delta k \\ \epsilon_{IL}^{n+1} = \epsilon_{IL}^n + \delta\epsilon \end{cases}$$

Table 1
Mesh grid used – DLR-TIC.

Mesh	Nozzle ($N_x \times N_y$)	$Jet(N_x \times N_y)$	Bottom domain ($N_x \times N_y$)
$\mathcal{M}_1$	388 × 200	308 × 484	87 × 165
$\mathcal{M}_2$	269 × 120	177 × 334	60 × 115
$\mathcal{M}_3$	403 × 190	261 × 434	90 × 145

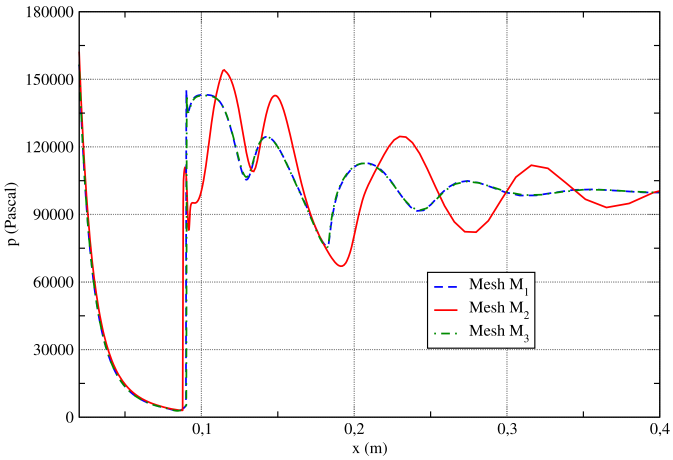

Fig. 6. Axial pressure for the three mesh grids – DLR-TIC.

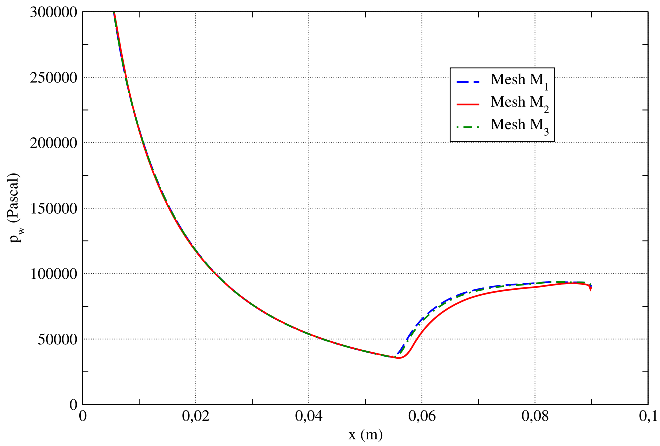

Fig. 7. Wall pressure for the mesh grids tested – DLR-TIC.

4. Grid independence

Only the study of the grid independence of DLR-TIC flow is presented. The influence of grid refinement was studied on three different meshes (see Table 1). The computed results are compared with axial pressure (Fig. 6), wall pressure (Fig. 7), and y^+ distribution for the first cell (Fig. 8). The results show that a grid convergence is reached. The simulations are then performed over a mesh grid in the streamwise and normal directions of 388 × 200 cells inside the nozzle and 308 × 484 cells outside of the nozzle. Then, the mesh grid used is $\mathcal{M}_1$. In the normal direction, near the nozzle wall region, the mesh is kept fine to have a y^+ value, for the first cell, less than 1 (Fig. 8).

5. Discussions – DLR-TIC

The wall pressure measurement profile and the computed one are represented in Fig. 9. One can observe the underprediction of the separation point abscissa and of the shock/boundary layer interaction. The shock separation structure occurs early in the divergent of the nozzle. The backflow or recirculation flow is found behind the separation shock near the nozzle wall. It is exhibited in skin friction profile (see Fig. 10). Like with the other nozzle flows [2] and [3], a little recirculation

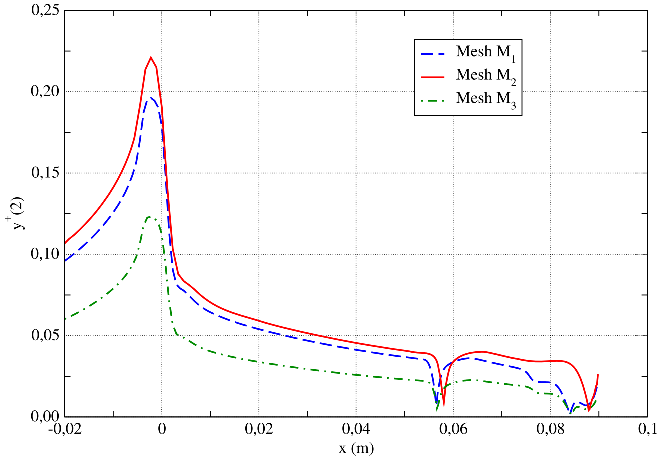

Fig. 8. y^+ value for the first cell near the nozzle wall for the three mesh grids – DLR-TIC.

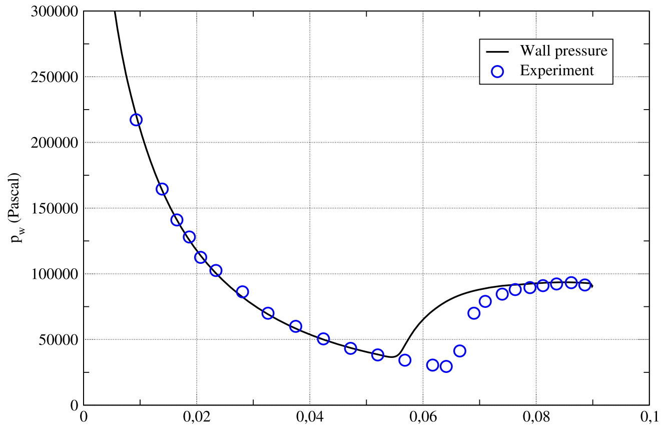

Fig. 9. Wall pressure – DLR-TIC.

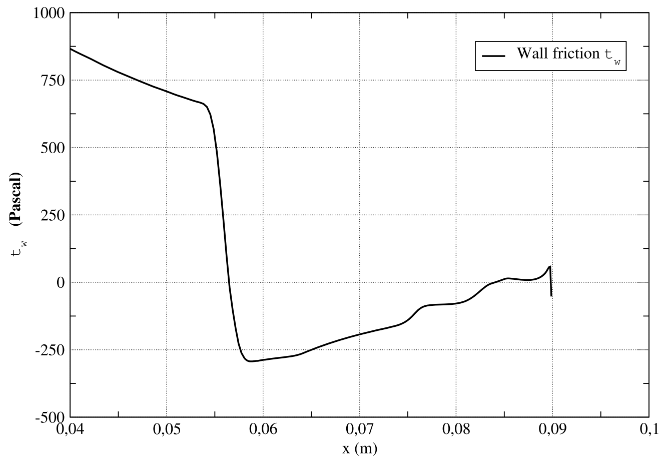

Fig. 10. Wall friction τ_w – DLR-TIC.

bubble is found near the nozzle lip where the skin friction becomes positive (see Fig. 12). All numerical results show a separation flow that continues as a free jet, typical of a free shock separation pattern. The separation shock reflects back into the symmetry axis with a Mach effect that leads to a lambda shock system produced by three shocks: the Mach disk, the incident, and the reflected shocks. These shocks interact on a point called triple point from where the slipstream em-

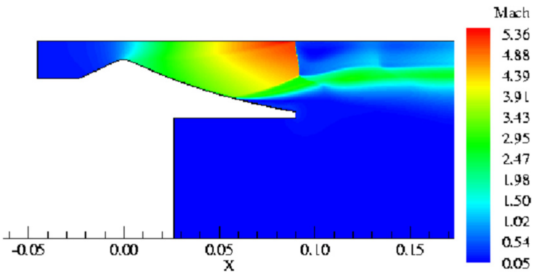

Fig. 11. Mach distribution – DLR-TIC.

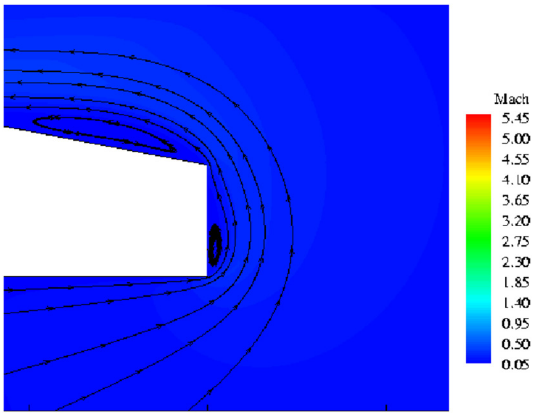

Fig. 12. Zoom Mach distribution – DLR-TIC.

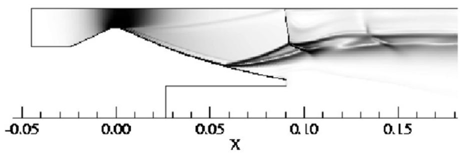

Fig. 13. Numerical Schlieren – DLR-TIC.

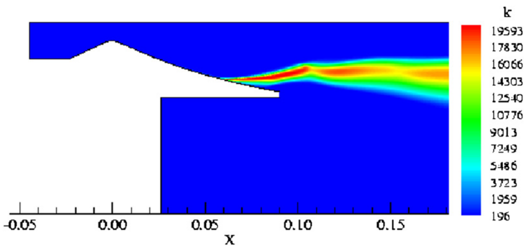

Fig. 14. Kinetic distribution – DLR-TIC.

anates. The shock/boundary layer interaction and the separation structure occur in the divergent (see Fig. 11, Fig. 13 and Fig. 15). Upstream of the shock structure, turbulence appears only close to the wall of the divergent part of the nozzle. Far from this wall, in the central region of the nozzle, the flow is rather inviscid. Thus, the turbulent boundary layer develops along this nozzle wall, and its thickness does not stop growing up to the separation point. The turbulence is regenerating downstream of the separation shock, in the mixing layer between the supersonic jet and the recirculation flow field. This is clearly visible in Fig. 14, which exhibit the turbulent energy contour k. The last turbulent quantity, in the mixing layer, reaches high values, and the flow is then fully turbulent. The numerical simulation, for the chosen nozzle pressure ratio, using the perfect gas assumption leads to the free shock separation pattern. One can observe that the DLR-TIC nozzle flow has been studied by Gross et al. [6] and Stark et al. [7].

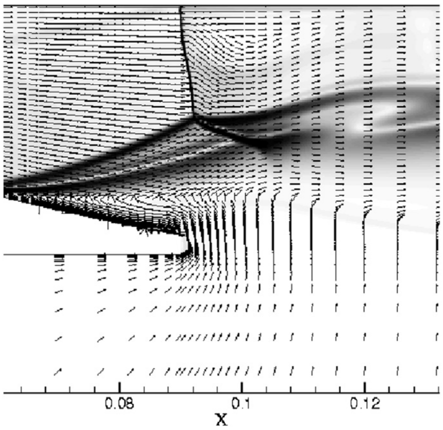

Fig. 15. Velocity vectors and numerical Schlieren – DLR-TIC.

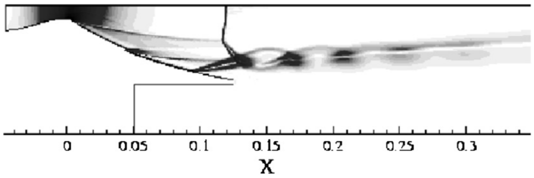

Fig. 16. Numerical Schlieren – ONERA-TOC.

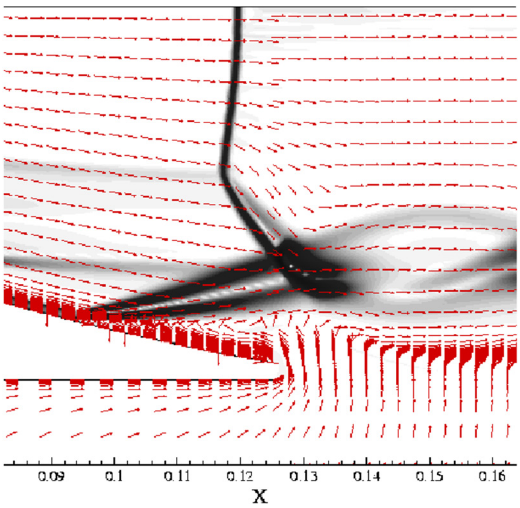

Fig. 17. Velocity Vectors and numerical Schlieren – ONERA-TOC.

6. Discussions – ONERA-TOC

The operating gas used here is a hot air at a stagnation temperature close to $T_c = 324$ K. For the stagnation pressure $p_c = 43.2$ bar, the condensation of the oxygen of air does not occur. The condensation phenomenon is then avoided in a present overexpanded ONERA-TOC nozzle flow at $NPR = p_c/p_a = 50$. The results show clearly in Figs. 16, 17, 18, and 19 a restricted shock separation with a cap-shock pattern. This shock structure does not exhibit the recirculation bubble downstream of the Mach disk and does not show the reattachment of the boundary layer. The measurements campaign on the plume of the same ONERA-TOC nozzle realized by Reijasse et al. [13] confirm the existence of the little vortex downstream of the Mach disk. The numerical simulations of the ONERA-TOC nozzle flow [13] show an RSS pattern without reattachment. It seems that the back-facing step in divergent prevents the separated flow from reattaching. Our computation reproduces the non-reattachment of the boundary layer and is in agreement with the experimental results of wall pressure (see Fig. 20). The NPR associated with the present nozzle flow locates the separation point near the nozzle's exit lip, and the shock structure pattern resulting is stable, without beating and without the longitudinal oscillation movement that appears in the

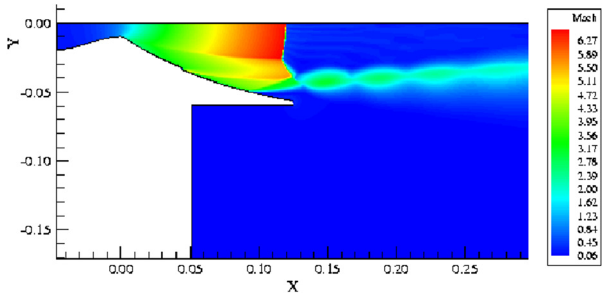

Fig. 18. Mach distribution – ONERA-TOC.

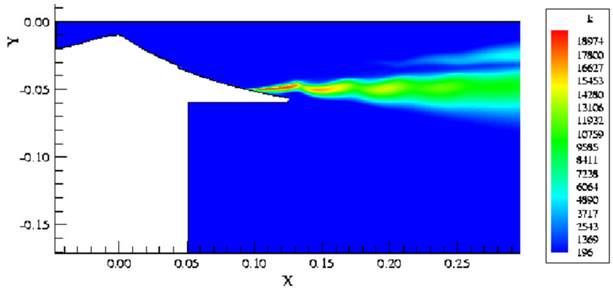

Fig. 19. Kinetic distribution – ONERA-TOC.

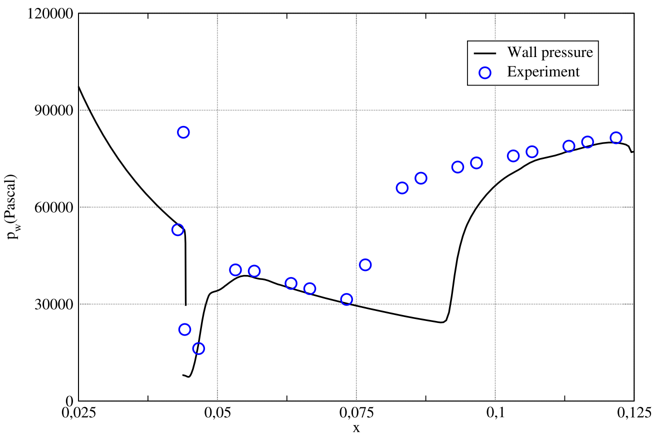

Fig. 20. Wall pressure – ONERA-TOC.

LEA-TOC nozzle [11] and [3]. For film cooling, the separation point at similar pressure ratio is located far more upstream than in the case of no film cooling [14].

7. Conclusions

A computational investigation of turbulent nozzle flow separation has been performed. The truncated ideal contour (DLR-TIC) and the thrust optimized contour (ONERA-TOC) nozzle flow, without wall film cooling, have been studied. The DLR-TIC nozzle flow shows that the condensation phenomenon does not appear by using the nitrogen as operating gas at a stagnation temperature and pressure close to, respectively, 270 K and 25 bar. For the nozzle pressure ratio $NPR = 25$, the separation region in the DLR-TIC nozzle extends from the separation point downwards the exit nozzle lip without any steady reattachment of the boundary layer. The classical free shock separation is then obtained in the DLR-TIC nozzle. The numerical simulation of the ONERA-TOC nozzle flow allowed us to obtain in this nozzle the restricted shock separation with the cap shock pattern. One can notice that our results show this RSS configuration to be without recirculation pocket downstream of the Mach disk and without reattachment of the boundary layer.

Acknowledgements

This work has been carried out in the framework of the French ATAC ("Aérodynamique des tuyères et arrière-corps") program with the financial support of CNES. We gratefully acknowledged fruitful discussions and exchange of data with the members of this project (CNES, ONERA, LEA, CORIA, IUSTI, SNECMA). Computational facilities were provided by CNRS–IDRIS ("Institut du développement et des ressources en informatique scientifique", Paris), CINES (Centre informatique national de l'enseignement superieur, Montpellier), and CRIANN (Centre régional informatique et d'applications numérique de Normandie, Rouen).

The subject of this work was taken from the test cases of the ATAC–FSCD Workshop "*After-Body and Nozzle Flows*", which is held at ESA–ESTEC Noordwijk, The Netherlands.

References

[1] S. Girard, Étude des charges latérales dans une tuyère supersonique surdétendue, Ph.D. thesis, University of Poitiers, France, 1999.
[2] C. Pilinski, A. Nebbache, Flow separation in a truncated ideal contour nozzle, J. Turbul. 5 (2004) 014.
[3] A. Nebbache, C. Pilinski, Pulsatory phenomenon in a thrust optimized contour nozzle, Aerosp. Sci. Technol. 10 (2006) 295–308.
[4] R.W. MacCormack, Current Status of Numerical Solutions of the Navier–Stokes Equations, AIAA paper 85-0032, 1985.
[5] F.R. Menter, Two-equation eddy-viscosity turbulence models for engineering applications, AIAA J. 32 (8) (1994) 1598–1605.
[6] A. Gross, C. Weiland, Investigation of Shock Patterns and Separation Behavior of Several Subscale Nozzles, AIAA paper 2000-3293, 2000.
[7] R.H. Stark, B.H. Wagner, Experimental Flow Investigation of a Truncated Ideal Contour Nozzle, AIAA paper 2006-5208, 2006.
[8] C.L. Chen, S.R. Chakravarthy, C.M. Hung, Numerical investigation of separated nozzle flows, AIAA J. 32 (9) (1994) 1836–1843.
[9] M. Frey, G. Hagemann, Status of Flow Separation Prediction in Rocket Nozzles, AIAA Paper 98-3619, 1998.
[10] L.H. Nave, G.A. Coffey, Sea Levels Side Loads in High-Area-Ratio Rocket Engines, AIAA Paper 73-1284, 1973.
[11] N.A. Thi, H. Deniau, S. Girard, T. Alziary de Roquefort, Unsteadiness of flow separation and end-effects regime in a thrust-optimized contour rocket nozzle, Flow Turbul. Combust. 71 (2003) 161–181.
[12] M. Onofri, F. Nasuti, The Physical Origins of Side-Loads in Rocket Nozzles, AIAA Paper 99-2587, 1999.
[13] P. Reijasse, F. Bouvier, P. Servel, Experimental and numerical investigation of the Cap–Shock structure in overexpanded thrust-optimized nozzles, in: D.E. Zeitoun, J. Periaux, J.A. Désidéri, M. Marini (Eds.), West East High Speed Flow Fields 2002. CIMNE Handbooks on Theory and Engineering Applications of Computational Methods, Barcelona, Spain, 2002.
[14] P. Reijasse, M. Frey, O. Haidn, Flow physics and side loads in highly over-expanded rocket nozzles, in: ODAS 2000, 2nd ONERA-DLR Aerospace Symposium, Berlin, Germany, 15–16 June 2000.
[15] C. Hirsch, Numerical Computation of Internal and External Flows, John Wiley & Sons, 1988.
[16] I. Shih Chang, One-and-Two-Phase Nozzle Flows, Report number SD-TR-80-26, The Aerospace Corporation, El Segundo, CA, USA, 1980.
[17] R.W. MacCormack, The Effect of Viscosity in Hypervelocity Impact Cratering, AIAA Paper 69-354, May 1969.